OCEANOGRAPHY

Bioinspired polarization vision enables underwater geolocalization

Samuel B. Powell,[1,2] Roman Garnett,[1] Justin Marshall,[2] Charbel Rizk,[3] Viktor Gruev[4,5]*

With its never-ending blue color, the underwater environment often seems monotonic and featureless. However, to an animal with polarization-sensitive vision, it is anything but bland. The rich repertoire of underwater polarization patterns—a consequence of light's air-to-water transmission and in-water scattering—can be exploited both as a compass and for geolocalization purposes. We demonstrate that, by using a bioinspired polarization-sensitive imager, we can determine the geolocation of an observer based on radial underwater polarization patterns. Our experimental data, recorded at various locations around the world, at different depths and times of day, indicate that the average accuracy of our geolocalization is 61 km, or 6 m of error for every 1 km traveled. This proof-of-concept study of our bioinspired technique opens new possibilities in long-distance underwater navigation and suggests additional mechanisms by which marine animals with polarization-sensitive vision might perform both local and long-distance navigation.

INTRODUCTION

Navigation using photoreceptor arrays specifically sensitive to patterns of the polarization of light in the sky is well documented in terrestrial animals, especially among arthropods such as ants, bees, crickets, dung beetles, and spiders (1–3). Honey bees journeying to and from hives rely on the predictable pattern of polarized light relative to the Sun's position, as noted by von Frisch (4) and Rossel and Wehner (5). This line of research has been recently extended to vertebrates: Longer-range migratory birds may use polarization patterns in the sky during sunrise and sunset to calibrate their magnetic compasses (6, 7). The underwater environment is another less explored area with highly structured polarization patterns down to at least 200 m, as first discovered by Talbot Waterman in 1954 (8). Although more than half a century has passed since Waterman's seminal publication, the scientific community seems to be divided about the true state of underwater polarization patterns and their usefulness. Scientists from various backgrounds, ranging from computer vision (9) and remote sensing to marine biology (10–12), argue that underwater light is almost or completely horizontally polarized based on either incomplete or incorrect underwater measurements and physical models. However, uniformly across the board, scientists have agreed and demonstrated that marine animals can use polarization patterns of the sky as viewed from underwater as a compass for navigation purposes (13, 14). Here, we demonstrate that underwater polarization light patterns not only are highly structured and dependent on the position of the Sun but also can be used for geolocalization purposes—a much more complicated and complete task than performed by a compass when it comes to navigation in underwater environments.

Two optical phenomena, light scattering and refraction, are mostly responsible for the underwater polarization patterns (8, 15, 16). As shown in Fig. 1, light from the Sun and sky (itself a product of scattered sunlight) enters the water by refracting through the surface. The refrac-

tion bends the light such that the image of the celestial hemisphere is compressed into an approximately 97° cone known as Snell's window. The transmitted light waves are preferentially polarized in the plane of the incident and refracted rays. The bulk of the light outside of Snell's window is refracted sunlight that has scattered from the water itself, but some of it is internally reflected light from the underside of the water's surface or reflected light from the seafloor (17). Scattering events partially polarize the light perpendicular to the plane of the incident and scattered rays, which produces a general trend of polarization perpendicular to the refracted ray (18). Figure 1B shows simulated underwater polarization patterns produced by this combination of refraction and single scattering for different Sun elevations. The background polarization patterns are highly variable and depend on the Sun's elevation and viewing angle of the observer. In certain situations, particularly when the Sun is low in the sky, it is possible for the polarization effect of the refraction to cancel or even to dominate that of the scattering. This causes "neutral points" in the polarization state of the light field facing the Sun and away from it, where the partial polarization drops to zero and the polarization angle abruptly transitions from horizontal to vertical (19). As the Sun's elevation drops below 40° above the horizon, skylight contributes an increasing fraction of the light incident on the water's surface (20). Although this effect was not included in our model because of computational complexity issues, it would be straightforward to add given sufficient computing power. In addition, at increasing depth or decreasing water clarity, multiply scattered light becomes more prevalent—this increases the homogeneity of the observed polarization states, resulting in less partial polarization and in polarization angles that are closer to horizontal. However, these effects are only significant beyond an optical depth of about 4, or about 2.35 times the Secchi disc visibility (19), and Sun-dependent patterns in the polarization angle have been observed as deep as 200 m (21).

The intensity and partial polarization of underwater light are highly sensitive to many environmental factors in addition to the Sun's position, including atmospheric conditions, water quality, and depth (22). However, the in-water patterns in the polarization angle (also known as the e-vector angle) are less sensitive to perturbations, including surface waves, and thus serve as a stable proxy for the Sun's position (16, 19, 23). Many marine animals are known to have polarization-sensitive vision, which has a variety of hypothesized uses, from improving visual contrast for predator and prey detection to covert communication (24–26).

[1]Department of Computer Science and Engineering, School of Engineering and Applied Science, Washington University in St. Louis, St. Louis, MO 63130, USA. [2]Sensory Neurobiology Group, Queensland Brain Institute, University of Queensland, St. Lucia, Queensland 4072, Australia. [3]Department of Electrical Engineering and Computer Engineering, Johns Hopkins University, Baltimore, MD 21218, USA. [4]Beckman Institute for Advanced Science and Technology, University of Illinois at Urbana-Champaign, Urbana, IL 61801, USA. [5]Department of Electrical and Computer Engineering, University of Illinois at Urbana-Champaign, Urbana, IL 61801, USA.
*Corresponding author. Email: vgruev@illinois.edu
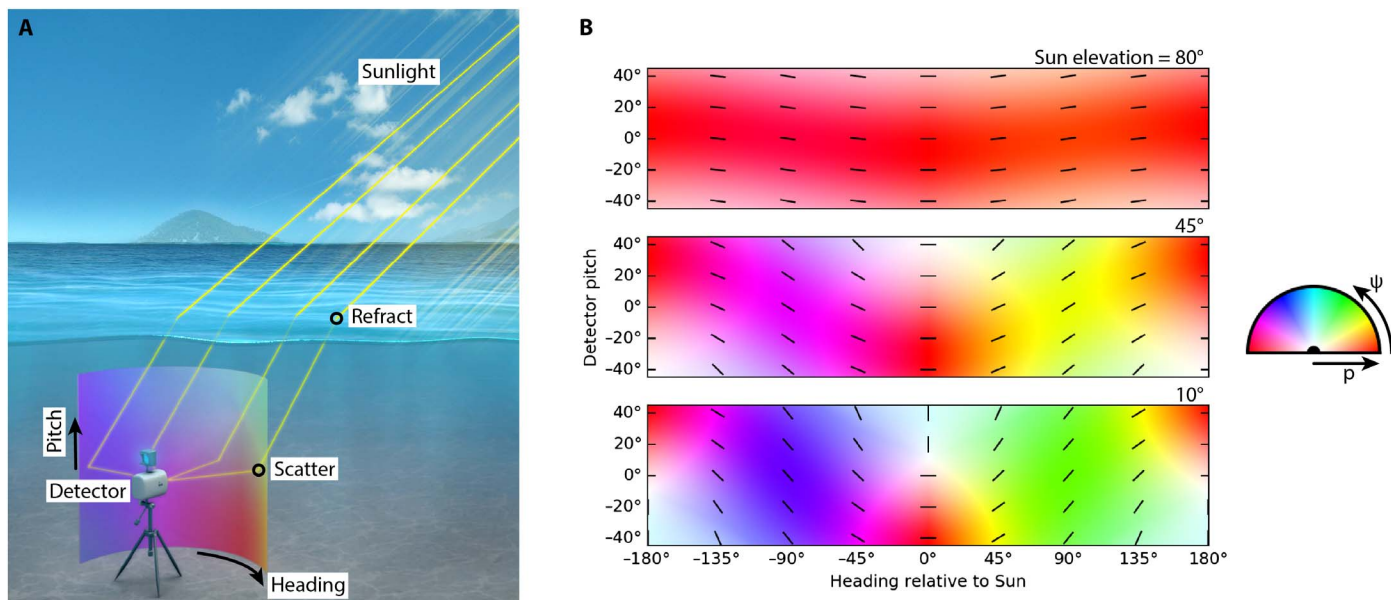
Fig. 1. Schematic of in-water polarization patterns. (**A**) The cylinder shows the polarization states that the detector observes, in false color. (**B**) Polarization states predicted by the single-scattering model, in false color (see key at right), for Sun elevations of 10°, 45°, and 80° above the horizon. For clarity, lines oriented at the polarization angles are overlaid on the graphs. Neutral points in the polarization occur where the polarization state of the scattering event cancels that of the refraction.

In addition, several works have focused on how salmonids could use the polarization patterns of the sky for orientation (27).

We hypothesize that, based on the underwater polarization patterns, the Sun's heading and elevation angles can be determined and hence the position of the observer can be estimated with accurate knowledge of time and date. To test this hypothesis, we collected data for inferring the Sun's position from underwater polarization angles using a bioinspired, visible-spectrum imaging polarimeter (28). The sensor mimics the polarization-sensitive vision system of the mantis shrimp by integrating various polarization optics within individual pixels of a camera. More specifically, polarization filters composed of parallel aluminum nanowires (140 nm thick × 70 nm wide) are aligned and deposited onto each pixel of a low-noise, 2-megapixel charge-coupled device image sensor. Similar to its biological counterpart, the pixelated polarization filters are oriented at set angles of 0°, 45°, 90°, and 135° in a repeating 2 × 2 pattern across the focal plane. This enables the polarimeter to capture intensity, partial polarization, and polarization angle images. We paired our bioinspired polarization camera with an electronic compass and tilt sensor within an underwater housing to measure the underwater polarization angles versus heading at a variety of sites, depths, and times of day (see Materials and Methods).

RESULTS AND DISCUSSION

Figure 2 shows several example measurements of the underwater polarization patterns compared to the output of a single-scattering model. The model agrees with the measurements when the Sun is at least 40° above the horizon. At lower elevations, contributions from the polarization patterns of the sky, among others, influence the overall underwater polarization pattern, and these physical phenomena are not captured in our model. To infer the Sun's position at different sites around the world and various times of the day, we used a general-purpose optimization algorithm to match the measured polarization angle pat-

terns against the predictions of a basic single-scattering model of underwater light (Fig. 3). For Sun elevation angles that are at least 40° above the horizon, the estimated Sun's heading and elevation angle had root mean square (RMS) errors of 8.57° and 5.82°, respectively, and a global positioning RMS error of 817 km.

The smoothly varying nature of the residuals (Fig. 2B) indicates that there are additional dependencies between the underwater polarization angle and the Sun's position that the single-scattering model does not capture. We incorporate these dependencies into our system by using a k-nearest-neighbors (kNN) regression to estimate the residuals of the model evaluated at the Sun's true position, as a function of the naïvely estimated Sun position. By subtracting the estimated residuals from our measurements during a second phase of inference, we can remove a significant amount of error: The RMS errors of the Sun's heading and elevation were reduced from 30 and 50% to 6.02° and 2.92°, respectively, and the global position RMS error improved from 46% to 442 km. Figure 3 shows the distribution of global position estimates and the improvements introduced by the kNN regression from experiments performed at the Lizard Island Research Station in northeastern Australia.

The model performance decreases as the Sun approaches the horizon, likely because the model does not include skylight, which contributes an increasingly large fraction of the light hitting the ocean's surface as the Sun drops below 40° above the horizon (20). When we include this low-elevation data, our naïve inference method achieves RMS errors of 9.22°, 8.07°, and 2915 km in Sun heading, Sun elevation, and global position, respectively. Incorporating the kNN residuals reduces these by 41, 23, and 32% to 5.46°, 6.23°, and 1970 km, respectively. Curiously, the accuracy of the kNN heading estimates improves when the low-elevation data are included, possibly because the polarization angle patterns develop a very strong gradient facing the Sun's heading. However, the lack of improvement in the Sun elevation estimate renders this improvement moot for purposes of global positioning (for performance statistics, see fig. S1).
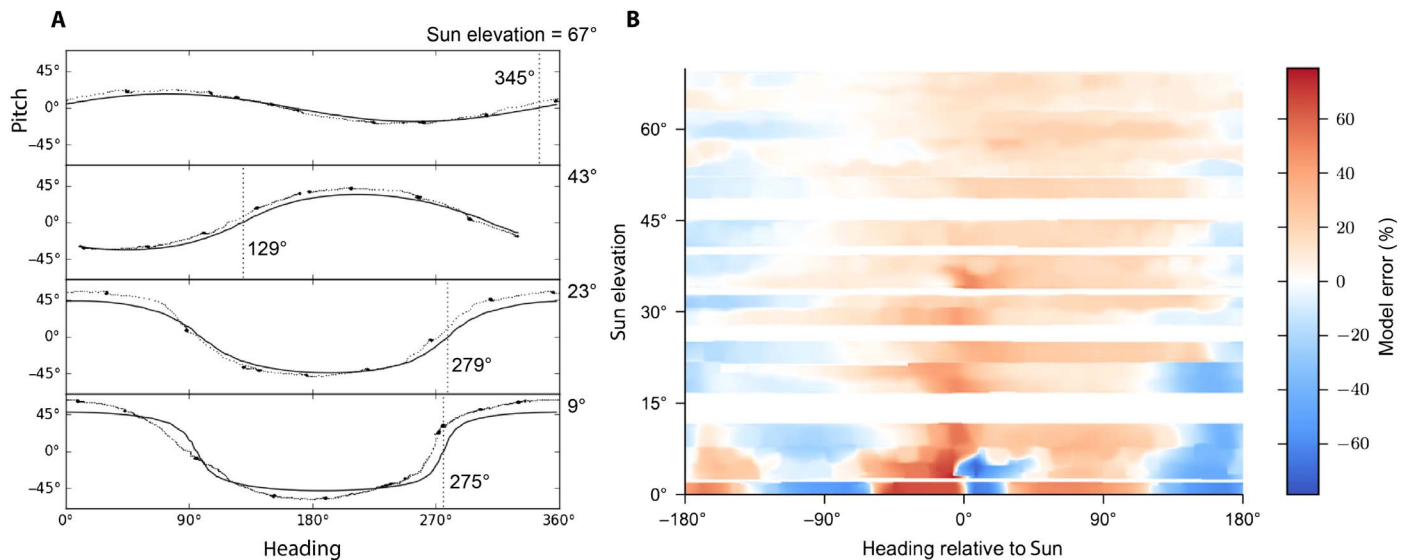
Fig. 2. Example measurements and residuals. (**A**) Polarization angle measurements from four experiments at varying Sun elevations. Measurements are indicated by dots; model predictions, by solid lines; the heading to the Sun, by the vertical dotted lines. (**B**) Differences between each measurement and the single-scattering model prediction, indicated by color. The smoothly varying nature of the residuals indicates additional dependencies between the underwater polarization angle and the Sun's position that the single-scattering model does not capture.
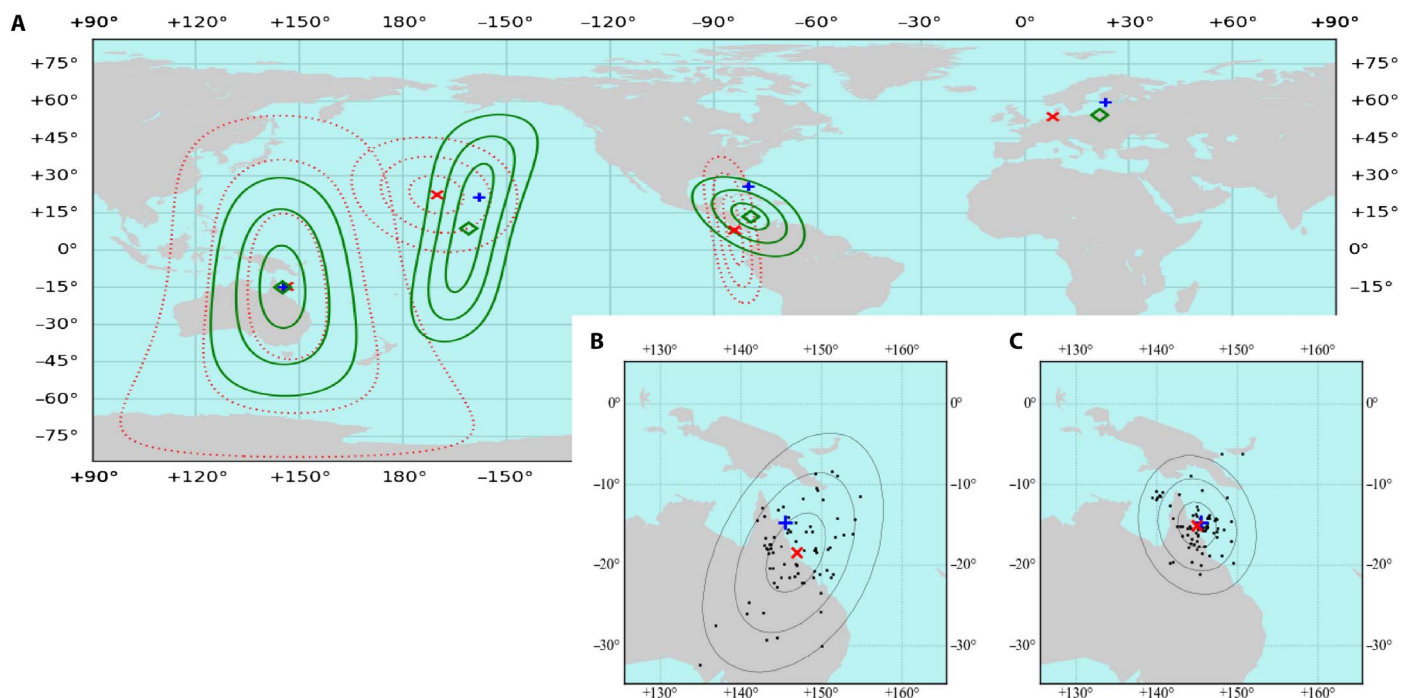

Fig. 3. Maps of position estimates. (**A**) World map of all position estimates. The blue pluses show the locations of the measurement sites, the red exes and dotted contour lines show the centroid and distribution of position estimates using just the single-scattering model for inference, and the green diamond and contours show the centroid and distribution of position estimates using the *k*NN method. The contours are at 1, 2, and 3 SDs from the centroid. Too few data were collected in Finland to estimate the SD contours. (**B** and **C**) Maps of position estimates from data taken at the Lizard Island Research Station when the Sun was at least 40° above the horizon, using only the single-scattering model (B) or the *k*NN method (C). The blue pluses show the location of the collection site, black dots are individual position estimates, and the red exes show the mean position estimate. The concentric curves are at 1, 2, and 3 SDs from the mean.

Although these errors may seem impractically large—following a heading 6° off course would result in a 105-m error after traveling 1 km—the RMS statistic includes a measure of the variance. When navigating with a noisy compass, one would use the average reading over time, not pick a single heading and follow it blindly. When the Sun's elevation is above 40°, the mean heading error was just 0.38° (6.6 m over 1 km), which is commensurate with the polarization compass abilities of the desert ant (*29*). In a similar fashion, it is more realistic
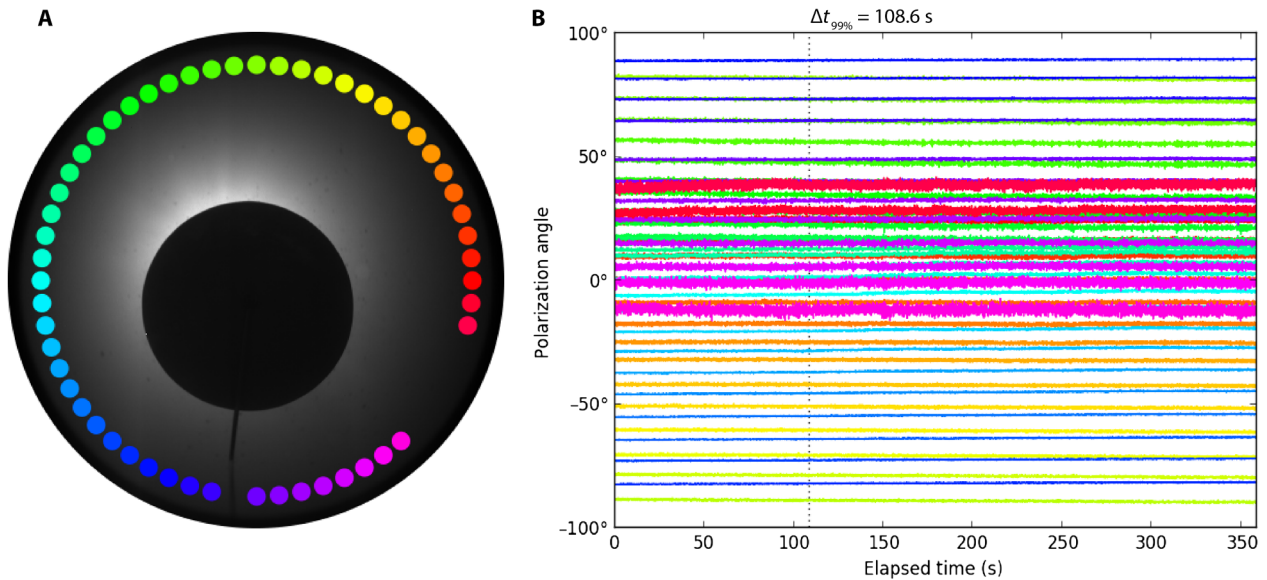
Fig. 4. Example sensitivity data. (**A**) Intensity image taken during a sensitivity experiment performed during the morning. The camera is set vertically, with a disc to block the Sun. The colored circles around the periphery show the regions over which the polarization angles are measured. Regions with partial polarization less than 5% were rejected. (**B**) Polarization angles measured during the sensitivity experiment; colors correspond to the regions shown in (A). The polarization angles vary almost linearly at the time of day the data were recorded. The vertical dotted line shows how long it takes the angles to change with 99% confidence.
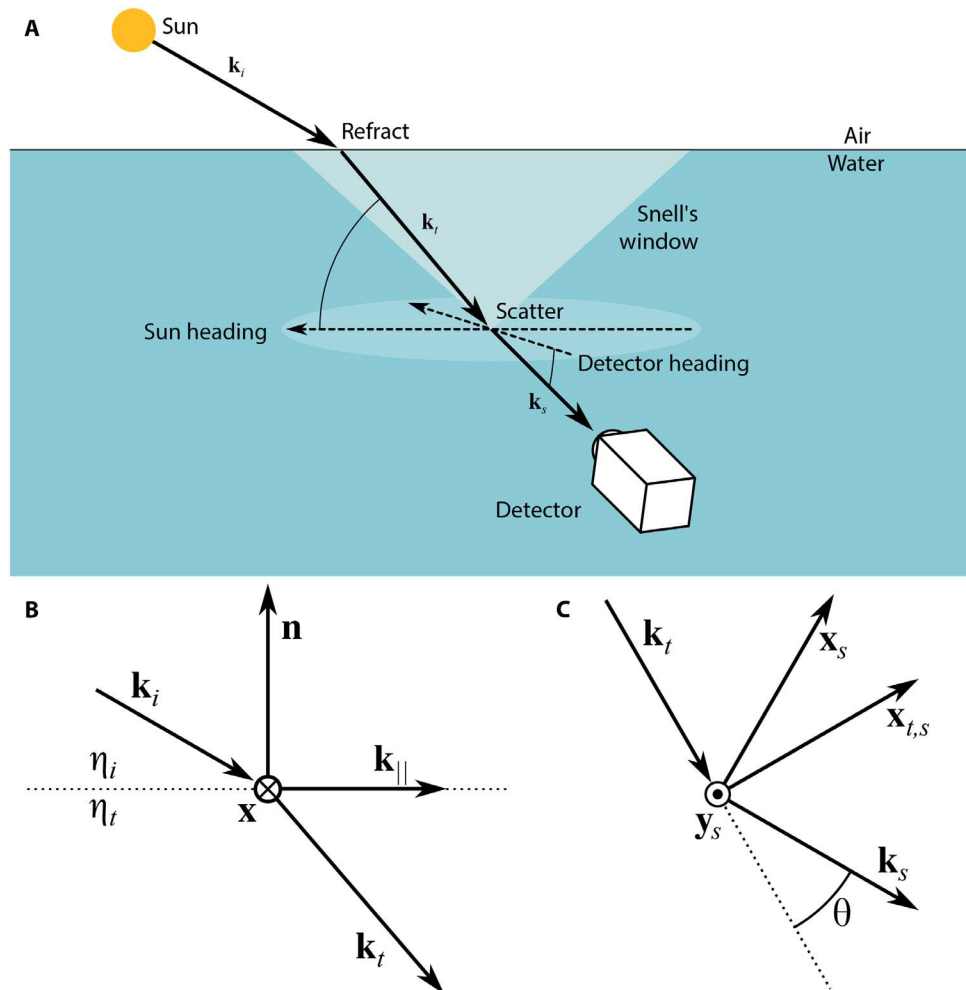
Fig. 5. Model schematics. (**A**) Single-scattering model geometry. (**B**) Refraction-event geometry. (**C**) Scattering-event geometry.

to consider the average of our global position estimates rather than treat them independently. As shown in Fig. 3, the centroid of position estimates performed in northern Australia is only 61 km from the true measurement location.

In addition to testing the inference algorithm on experimental data, we also performed a sensitivity study of our instruments (see Materials and Methods and Fig. 4). We wanted to determine the minimum distance between two sites required for our camera to detect significant differences in their underwater polarization patterns. However, approaching this problem directly would require moving two identical instruments to various distances from each other and collecting synchronized recordings, which is a technically infeasible task. Instead, we answered a slightly different question: If we place a polarization instrument underwater that is capable of instantaneously recording a 360° field of view, how long does it take the Sun to travel far enough for the camera to register a significant difference in the background polarization pattern? Once we determine the time it takes to detect a significant difference in the background polarization pattern, the distance (that is, solar angle) that the Sun has traveled can be computed. The solar angle that we can measure is the equivalent to the difference between solar angles at two locations at the same time. In one experiment, the instrument was capable of detecting, with 99% confidence, changes to the underwater polarization angle pattern in calm conditions caused by a 0.31° movement of the Sun, which corresponds to a movement of 35 km along the latitude where the sensitivity measurements were performed. Another experiment, recorded over a 9-hour period under calm conditions, yielded an average sensitivity of 42 ± 4.1 km (mean ± SD). The Sun's elevation varied from 30° to 71° over the course of the experiment, which indicates that the noise characteristics of the polarization signals are stable over long periods and under a variety of solar elevations. We also observed that under windy conditions (~35 km/hour), wave action caused a marked increase in noise levels in the polarization angles and reduced the overall system sensitivity to 116 km (see fig. S2). Unlike the instrument's measurement noise, however, the noise introduced by surface waves appears to be highly spatially correlated across the sensor, which could enable more advanced statistical techniques to mitigate it. This implies that a majority of the positioning error in our system is due to model errors rather than sensor performance.

Our results show that underwater polarization angles can reasonably serve as a solar compass for animals with polarization-sensitive vision and can also be used to determine global location. Considering the uniformity of the polarization properties of oceanic waters from around the world, we believe that our method will generalize well to locations beyond our measurement sites (30). This study also provides insight into an additional navigation method for animals with polarization-sensitive vision.

MATERIALS AND METHODS
Instrument design
Two underwater polarization video cameras were used for this work. The polarization image sensors were mounted in Imperx Bobcat GEV camera bodies with Canon EF-S 18- 55 mm lenses. The lens mounts were customized to provide electronic control of the lenses. Each video camera included a PNI Sensor Corporation TCM MB electronic compass module. These modules contain both a three-axis magnetometer and a three-axis accelerometer and provide magnetic heading, roll, and pitch information at 30 Hz over a digital interface with an RMS error of less than 0.5°.

The polarization sensor and compass module were both housed in a Light and Motion Bluefin VX2000 underwater housing along with an ADL Embedded Solutions QM67PC single-board computer running CentOS Linux. A small HDMI (high-definition multimedia interface) monitor was attached to the system for visual feedback, and a PJRC Teensy 3.2 microcontroller was used to translate the housing controls and Canon lens protocol to and from the USB (universal serial bus). The computer was programmed with a real-time user interface to allow a diver to control the system while viewing the live polarization video. The software records all data emitted by the sensors, including microsecond-resolution time stamps, into standard HDF5 files for maximum reliability and compatibility. Because of the nature of the computer's clock, the time stamps have very low jitter but are accurate to within approximately 2 s of UTC (coordinated universal time).

For the sensitivity experiment, one of the instruments was modified to accept an Aquatica 4″ glass dome port, and the Canon lens was replaced with a Fujinon FE185C057HA-1 fish-eye lens. See fig. S3 and movie S1 for photos and video of the system in use, respectively.

Polarimetric calibration
The polarimeters were calibrated by collecting images of a white flat field through a Newport 20LP-VIS-B 2″ linear polarization filter. The flat field was produced by illuminating two layers of opal-glass diffuser with a tungsten halogen lamp via a fiber-optic light pipe. Unwanted infrared illumination was blocked with a heat-absorbing glass disc. The flat field was set to five different intensities, and at each, the polarization filter was rotated through six angles from 0° to 180°; 100 polarization images were averaged for each intensity-angle pair to reduce the effects of temporal noise.

The flat-field images were used to compute dark offsets and polarimetric calibration matrices for each 2 × 2 square of pixels (31). These calibration matrices normalize the relative intensity and partial polarization responses across the focal plane and provide absolute calibration of the measured polarization angles.

Sun position inference data collection
Polarization data for Sun position inference was collected at the Lizard Island Research Station (Australia), the Hawaiian Electric Beach Park (Hawaii), Miami (Florida), and the Tvärminne Zoological Station (Finland) (see Fig. 3). The measurements were performed by scuba divers at depths from 2 to 20 m at various times of the day from sunrise to sunset. Dive site locations were recorded at the surface with a Garmin Oregon 700 GPS receiver. The imaging instrument was mounted on a tripod such that it rotated freely about the vertical axis, and pitched such that neither the water surface nor the seafloor was visible in the center of the field of view. The operating diver then measured the instrument depth with a dive computer. For each recording, the instrument was rotated once around the vertical axis, pausing approximated every 45° to allow the compass and tilt sensor to settle. Recordings were typically less than 2 min in duration, and anywhere from 2 to 10 recordings were collected per dive depending on the circumstances.

To process these recordings, we polarimetrically calibrated each video frame and cropped it to a 100 × 100–pixel region at the center of the field of view. We computed the average Stokes vector over the region and extracted the polarization angle from it. Frames were rejected if they contained the seafloor, water surface, objects, bubbles, or animals in the region of interest, or if the Sun was visibly shaded by clouds or nearby boats. The compass measurements were smoothed by applying a low-pass sinc filter with a −3-dB frequency of 1.35 Hz.

Single-scattering model

Our single-scattering model of underwater polarization states is based on the Mueller-Stokes formalism of representing polarized light (see Fig. 5). A ray of polarized light is represented by a wave vector $\mathbf{k} \in \mathbb{R}^3$ (rad/m), encapsulating its wave number and direction of travel, and a Stokes vector $\mathbf{S} \in \mathbb{R}^4$ (W/m²), which encapsulates its intensity and polarization state. In addition, we must track a vector $\mathbf{x} \in \mathbb{R}^3$, perpendicular to $\mathbf{k}$, which indicates the direction corresponding to a polarization angle of zero. Optical events that modify the polarization state of the light are modeled by multiplying the Stokes vector by a Mueller matrix $\mathbf{M} \in \mathbb{R}^{4 \times 4}$.

The first optical event of our model is the refraction of sunlight ($\mathbf{k}_i, \mathbf{x}_i, \mathbf{S}_i$) through the water's surface. The air-water interface is defined by the surface normal $\mathbf{n}$ and the real indices of refraction of the air and water, η_i and η_t. The transmitted light ($\mathbf{k}_t, \mathbf{x}_t, \mathbf{S}_t$) is computed per Snell's law and Fresnel's equations (18), with the $\mathbf{x}$ vectors lying in the water surface

$$\mathbf{k}_t = \mathbf{k}_a - \mathbf{n}\sqrt{(\eta_t/\eta_i)^2 \|\mathbf{k}_i\|^2 - \|\mathbf{k}_a\|^2}, \quad \mathbf{k}_a = \mathbf{k}_i - (\mathbf{k}_i \cdot \mathbf{n})\mathbf{n} \quad (1)$$

$$\mathbf{x}_t = \mathbf{x}_i = \mathbf{n} \times \mathbf{k}_i / \|\mathbf{n} \times \mathbf{k}_i\| \quad (2)$$

$$\mathbf{S}_t = \mathbf{M}_R \mathbf{S}_i \quad (3)$$

$$\mathbf{M}_R = \frac{1}{2}\begin{pmatrix} t_s^2 + t_p^2 & t_s^2 - t_p^2 & 0 & 0 \\ t_s^2 - t_p^2 & t_s^2 + t_p^2 & 0 & 0 \\ 0 & 0 & 2t_s t_p & 0 \\ 0 & 0 & 0 & 2t_s t_p \end{pmatrix},$$

$$t_s = \frac{2\mathbf{k}_i \cdot \mathbf{n}}{(\mathbf{k}_i + \mathbf{k}_t) \cdot \mathbf{n}}, \quad t_p = \frac{2\eta_i \eta_t \mathbf{k}_i \cdot \mathbf{n}}{(\eta_t^2 \mathbf{k}_i + \eta_i^2 \mathbf{k}_t) \cdot \mathbf{n}} \quad (4)$$

The second optical event is the scattering of the transmitted sunlight. The wave vector of the scattered light, $\mathbf{k}_s$, is the same magnitude as $\mathbf{k}_t$ but points to the detector. The typical coordinate system for representing scattering events has the $\mathbf{x}$ vectors of the incident and scattered light lying in the same plane as the wave vectors; thus, $\mathbf{S}_t$ must be rotated by a coordinate transform matrix $\mathbf{M}_{R \to S}$ before being multiplied by the scattering matrix $\mathbf{M}_S$. We model the polarization effects of scattering using the Rayleigh approximation but renormalized so that the intensity follows $\tilde{\beta}_{FF}(\theta)$ (sr⁻¹), the Fournier-Forand volume scattering phase function (17)

$$\mathbf{x}_s = \frac{\mathbf{k}_t \times \mathbf{k}_s \times \mathbf{k}_s}{\|\mathbf{k}_t \times \mathbf{k}_s \times \mathbf{k}_s\|}, \quad \mathbf{x}_{t,s} = \frac{\mathbf{k}_t \times \mathbf{k}_s \times \mathbf{k}_t}{\|\mathbf{k}_t \times \mathbf{k}_s \times \mathbf{k}_t\|} \quad (5)$$

$$\mathbf{S}_s = \mathbf{M}_S \mathbf{M}_{R \to S} \mathbf{S}_t \quad (6)$$

$$\mathbf{M}_S = \frac{\tilde{\beta}_{FF}(\theta)}{c_\theta^2 + 1}\begin{pmatrix} c_\theta^2 + 1 & c_\theta^2 - 1 & 0 & 0 \\ c_\theta^2 - 1 & c_\theta^2 + 1 & 0 & 0 \\ 0 & 0 & 2c_\theta & 0 \\ 0 & 0 & 0 & 2c_\theta \end{pmatrix},$$

$$c_\theta = \cos\theta, \quad \theta = \text{angle}(\mathbf{k}_t, \mathbf{k}_s) \quad (7)$$

Multiplying by $\tilde{\beta}(\theta)$ changes the units of $\mathbf{S}_s$ to (W·m⁻²·sr⁻¹); however, returning to (W·m⁻²) is not straightforward. This is because the volume scattering phase function is the ratio of the scattered radiant intensity per volume (W·sr⁻¹·m⁻³) to the incident intensity (W·m⁻²) normalized by the scattering coefficient per volume (W·m⁻³)/(W·m⁻²). Thus, we must multiply $\mathbf{S}_s$ by the scattering coefficient and scattering volume to yield a radiant intensity (W·sr⁻¹), which can then be multiplied by an area per solid angle to yield intensity again. These operations do not affect the polarization angle, so we neglect them.

Finally, the Stokes vector of the scattered light is transformed to the coordinate frame of the detector, with $\mathbf{x}$ to the right and polarization angles increasing in the counterclockwise direction, as viewed by the detector. The detected Stokes vector is thus

$$\mathbf{S}_d = \mathbf{M}_{S \to D} \mathbf{M}_S \mathbf{M}_{R \to S} \mathbf{M}_R \mathbf{S}_i \quad (8)$$

We assumed that the incident sunlight was unpolarized, so $\mathbf{S}_i = (1, 0, 0, 0)^T$, and computed the Sun's apparent position in the sky with Reda and Andreas's algorithm (32). When operating with magnetic headings, we used the National Oceanic and Atmospheric Administration's Enhanced Magnetic Model (33) to provide local fields.

Sun position inference

Our system infers the Sun's position in a two-phase process. During the first phase, an initial estimate of the Sun's angular position in the sky, $\hat{\rho}_s^{(1)} \in \mathbb{S}^2$, is obtained according to

$$\hat{\rho}_s^{(1)} = \text{argmin}\|\boldsymbol{\psi} \ominus \psi_m\left(\boldsymbol{\rho}_d, \hat{\rho}_s^{(1)}\right)\|_1 \quad (9)$$

where $\boldsymbol{\psi} \in \mathbb{S}^n$ is the vector of polarization angles measured at each detector orientation, $\rho_d \in \mathbb{S}^{2 \times n}$, and $\psi_m : \mathbb{S}^{2 \times n}, \mathbb{S}^2 \to \mathbb{S}^n$ is the single-scattering model. The L¹ norm is used to deemphasize outliers caused by measurement noise. The $\ominus$ operator indicates an element-wise angular difference

$$a \ominus b = (a - b + \tau/2) \, mod \, \tau - \tau/2, \quad a \, mod \, b = a - b\lfloor a/b \rfloor \quad (10)$$

where τ is the period of the angle (180° for polarization angles). Because the predictive power of the single-scattering model is limited, we use a kNN regression (34) over previously measured data to estimate the residuals of the single-scattering model, $\Delta\psi_m$, at the true Sun position as a function of the estimated Sun position

$$\Delta\hat{\psi}_m\left(\boldsymbol{\rho}_d, \hat{\rho}_s^{(1)}\right) \approx \boldsymbol{\psi} \ominus \psi_m(\boldsymbol{\rho}_d, \rho_s) \quad (11)$$

The second phase of the inference algorithm used the estimated residuals to remove model errors from the minimization to improve the inference results

$$\begin{aligned} \hat{\rho}_s^{(2)} &= \text{argmin}\|\boldsymbol{\psi} \ominus \Delta\hat{\psi}_m\left(\boldsymbol{\rho}_d, \hat{\rho}_s^{(1)}\right) \ominus \psi_m\left(\boldsymbol{\rho}_d, \hat{\rho}_s^{(2)}\right)\|_1 \\ &\approx \text{argmin}\|\psi_m(\boldsymbol{\rho}_d, \rho_s) \ominus \psi_m\left(\boldsymbol{\rho}_d, \hat{\rho}_s^{(2)}\right)\|_1 \end{aligned} \quad (12)$$

The global position of the measurement, $\hat{\rho}_g \in \mathbb{S}^2$, can be determined from the estimated Sun position as in

$$\hat{\rho}_g = \text{argmin} \, \text{arcdist}\left(\hat{\rho}_s, \rho_s(\hat{\rho}_g, t)\right) \quad (13)$$

where t is the time of the measurement and $\rho_s : \mathbb{S}^2, \mathbb{R} \to \mathbb{S}^2$ is a model of the apparent Sun position using magnetic headings, as described previously.

The inference algorithm was tested using the L-BFGS-B algorithm to solve the minimizations and the leave-one-out methodology to separate training from test data for the kNN regression. First, for each experiment, we computed $\hat{\rho}_s^{(1)}$, the naïve Sun position estimate, and $\Delta\psi_m = \psi - \psi_m(\rho_d, \rho_s)$, the single-scattering model residuals evaluated at the true Sun position. We then separated the data into groups based on collection site and date, and for each group, we generated a residual estimate function, $\Delta\tilde{\psi}_m(\rho_d, \rho_s)$, by training a kNN regression with the $\hat{\rho}_s^{(1)}$ and $\Delta\psi_m$ from all the data in the other groups. This residual estimate function was then used to compute the second-phase Sun position estimate, $\hat{\rho}_s^{(2)}$. We chose this methodology because it allows us to test the effects of the kNN regression in a data-efficient manner.

Statistics on the global position distance errors were performed assuming a normal distribution. Statistics on the Sun heading errors and Sun elevation errors were performed independently, assuming a wrapped normal distribution. The first moment of the population was used to estimate the mean and variance of the normal distribution underlying the wrapped normal

$$\bar{\theta} = \arg m_1(\theta), \quad \in \mathrm{var}(\theta) = -2 \log |m_1(\theta)|,$$
$$m_1(\theta) = \frac{1}{n}\sum_j e^{i\theta_j} \tag{14}$$

The RMS statistics were then computed using the mean and variance as

$$\mathrm{RMS}(\theta) = \sqrt{\bar{\theta}^2 + \mathrm{var}(\theta)} \tag{15}$$

Significance values were determined with a paired t test. Statistics on the global position estimates were performed by estimating the parameters of a Kent distribution using the maximum likelihood estimation method. Details are available in the online code listing.

Sensitivity analysis

The sensitivity analysis data were collected at Dique la Quebrada in Argentina, Xpu-ha in Mexico, and Ohrid in Republic of Macedonia. The instrument, configured with the fish-eye lens, was mounted vertically on a tripod. A metal disc was mounted on a small arm above the lens to block the Sun and prevent the image from blooming. The depth of the instrument, 2.5 m, was estimated by the diver. The longest continuous clean data segment from each session was used for analysis. In this case, the clean data were free from animals or foreign objects and were recorded while the Sun was not obscured by clouds.

These videos were processed by taking the average polarization state from circular regions placed every 6° of heading around the periphery of the image at approximately 7.5° above the horizontal plane. Data from regions where the partial polarization dipped below 5% were discarded. The short duration of the time series allows us to model the polarization angles using a Gaussian process with a linearly changing mean and stationary covariance

$$\psi(t) \in \mathbb{S}^n \sim \mathcal{N}(\psi_0 + \psi_1 t, \Sigma) \tag{16}$$

The parameters of the mean were estimated with a linear least-squares regression on the measured angles, unwrapped so that there are no discontinuities between 180° and 0°. The covariance matrix was estimated from the regression's residuals. We used the Mahalanobis distance metric to determine how long it takes for the mean to change such that it can be detected with a certain confidence. Because the mean of the process is a linear function in time, the Mahalanobis distance between means is

$$D_M(\bar{\psi}(t_a), \bar{\psi}(t_b)) = \sqrt{(\bar{\psi}(t_b) - \bar{\psi}(t_a))^T \Sigma^{-1}(\bar{\psi}(t_b) - \bar{\psi}(t_a))}$$
$$= |t_b - t_a|\sqrt{\psi_1^T \Sigma^{-1} \psi_1} \sim \sqrt{\chi_n^2} \tag{17}$$

The χ_n^2 distribution's inverse survival function gives us the minimum Mahalanobis distance beyond which we would reject the hypothesis that a sample was drawn from the distribution at time t_a with a given false rejection rate. We take advantage of the linear form of the distance to solve for the amount of time required for the mean polarization angle to change with 99% confidence

$$\Delta t_{99\%} = \frac{\sqrt{\mathrm{ISF}_{\chi_n^2}(1\%)}}{\sqrt{\psi_1^T \Sigma^{-1} \psi_1}} \tag{18}$$

Finally, because the change in polarization angles is driven by the movement of the Sun, we claim that, under similar conditions, the instrument can detect changes in the Sun position of the same magnitude as that which occurred over the $\Delta t_{99\%}$ interval during the experiment. We estimated the instrument's sensitivity to changes in location by computing the linear distance the earth rotates relative to the Sun over $\Delta t_{99\%}$ at the latitude of the experiment.

Computer codes

Code listings of our algorithms are available online at https://bitbucket.org/sbpowell/underwater-pol-nav. The code listings are written in Python, using NumPy, SciPy, and various libraries (35–38).

SUPPLEMENTARY MATERIALS

Supplementary material for this article is available at http://advances.sciencemag.org/cgi/content/full/4/4/eaao6841/DC1

fig. S1. RMS error statistics.
fig. S2. Sensitivity data recorded under windy conditions.
fig. S3. Camera hardware in use.
movie S1. Data collection with bioinspired polarization imaging sensor.

REFERENCES AND NOTES

1. T. Labhart, E. P. Meyer, Detectors for polarized skylight in insects: A survey of ommatidial specializations in the dorsal rim area of the compound eye. *Microsc. Res. Tech.* **47**, 368–379 (1999).
2. B. el Jundi, J. Smolka, E. Baird, M. J. Byrne, M. Dacke, Diurnal dung beetles use the intensity gradient and the polarization pattern of the sky for orientation. *J. Exp. Biol.* **217**, 2422–2429 (2014).
3. M. Dacke, T. A. Doan, D. C. O'Carroll, Polarized light detection in spiders. *J. Exp. Biol.* **204**, 2481–2490 (2001).
4. K. von Frisch, Gelöste und ungelöste Rätsel der Bienensprache. *Naturwissenschaften* **35**, 38–43 (1948).
5. S. Rossel, R. Wehner, The bee's map of the e-vector pattern in the sky. *Proc. Natl. Acad. Sci. U.S.A.* **79**, 4451–4455 (1982).
6. F. R. Moore, J. B. Phillips, Sunset, skylight polarization and the migratory orientation of yellow-rumped warblers, *Dendroica coronata*. *Anim. Behav.* **36**, 1770–1778 (1988).
7. R. Muheim, Behavioural and physiological mechanisms of polarized light sensitivity in birds. *Philos. Trans. R. Soc. B* **366**, 763–771 (2011).

8. T. H. Waterman, Polarization patterns in submarine illumination. *Science* **120**, 927–932 (1954).

9. Y. Y. Schechner, N. Karpel, Clear underwater vision, in *Proceedings of the 2004 IEEE Computer Society Conference on Computer Vision and Pattern Recognition*, Washington, DC, 27 June to 2 July 2004 (IEEE, 2004).

10. R. Wehner, Polarization vision—A uniform sensory capacity?. *J. Exp. Biol.* **204**, 2589–2596 (2001).

11. N. Shashar, S. Sabbah, T. W. Cronin, Transmission of linearly polarized light in seawater: Implications for polarization signaling. *J. Exp. Biol.* **207**, 3619–3628 (2004).

12. E. J. Warrant, N. A. Locket, Vision in the deep sea. *Biol. Rev.* **79**, 671–712 (2004).

13. T. H. Waterman, Reviving a neglected celestial underwater polarization compass for aquatic animals. *Biol. Rev.* **81**, 111–115 (2006).

14. A. Lerner, S. Sabbah, C. Erlick, N. Shashar, Navigation by light polarization in clear and turbid waters. *Philos. Trans. R. Soc. Lond. B* **366**, 671–679 (2011).

15. N. G. Jerlov, Oceanic light scattering properties related to dynamic conditions. *Opt. Eng.* **8**, 080389 (1970).

16. T. H. Waterman, W. E. Westell, Quantitative effect of the sun's position on submarine light polarization. *J. Mar. Res.* **15**, 149–169 (1956).

17. C. D. Mobley, E. Boss, C. Roesler, *Ocean Optics Web Book* (1994); www.oceanopticsbook.info/.

18. M. Born, E. Wolf, *Principles of Optics* (Cambridge Univ. Press, ed. 7, 1999).

19. V. A. Timofeeva, Optics of turbid waters (results of laboratory studies), in *Optical Aspects of Oceanography*, N. Jerlov, E. Steemann Nielsen, Eds. (Academic Press, 1974).

20. N. G. Jerlov, *Optical Oceanography* (Elsevier, 1968).

21. T. H. Waterman, Polarization of scattered sunlight in deep water. *Deep-Sea Res.* **3**, 426–434 (1955).

22. A. Ivanoff, T. H. Waterman, Factors, mainly depth and wavelength, affecting the degree of underwater light polarization. *J. Mar. Res.* **16**, 283–307 (1958).

23. Y. You, G. W. Kattawar, K. J. Voss, P. Bhandari, J. Wei, M. Lewis, C. J. Zappa, H. Schultz, Polarized light field under dynamic ocean surfaces: Numerical modeling compared with measurements. *J. Geophys. Res.: Oceans* **116**, C00H05 (2011).

24. G. Horváth, D. Varjú, *Polarized Light in Animal Vision: Polarization Patterns in Nature* (Springer, 2004).

25. P. C. Brady, A. A. Gilerson, G. W. Kattawar, J. M. Sullivan, M. S. Twardowski, H. M. Dierssen, M. Gao, K. Travis, R. I. Etheredge, A. Tonizzo, A. Ibrahim, C. Carrizo, Y. Gu, B. J. Russell, K. Mislinski, S. Zhao, M. E. Cummings, Open-ocean fish reveal an omnidirectional solution to camouflage in polarized environments. *Science* **350**, 965–969 (2015).

26. T. W. Cronin, N. Shashar, R. L. Caldwell, J. Marshall, A. G. Cheroske, T.-H. Chiou, Polarization vision and its role in biological signaling. *Integr. Comp. Biol.* **43**, 549–558 (2003).

27. D. C. Parkyn, J. D. Austin, C. W. Hawryshyn, Acquisition of polarized-light orientation in salmonids under laboratory conditions. *Anim. Behav.* **65**, 893–904 (2003).

28. T. York, S. B. Powell, S. Gao, L. Kahan, T. Charanya, D. Saha, N. W. Roberts, T. W. Cronin, J. Marshall, S. Achilefu, S. P. Lake, B. Raman, V. Gruev, Bioinspired polarization imaging sensors: From circuits and optics to signal processing algorithms and biomedical applications. *Proc. IEEE* **102**, 1450–1469 (2014).

29. D. Lambrinos, R. Möller, T. Labhart, R. Pfeifer, R. Wehner, A mobile robot employing insect strategies for navigation. *Robot Auton. Syst.* **30**, 39–64 (2000).

30. K. J. Voss, E. S. Fry, Measurement of the Mueller matrix for ocean water. *Appl. Optics* **23**, 4427–4439 (1984).

31. S. B. Powell, V. Gruev, Calibration methods for division-of-focal-plane polarimeters. *Opt. Express* **21**, 21039–21055 (2013).

32. I. Reda, A. Andreas, Solar position algorithm for solar radiation applications. *Solar Energy* **76**, 577–589 (2004).

33. A. Chulliat, P. Alken, M. Nair, A. Woods, S. Maus, *The Enhanced Magnetic Model 2015–2020* (National Centers for Environmental Information, National Oceanic and Atmospheric Administration, 2015).

34. N. S. Altman, An introduction to kernel and nearest-neighbor nonparametric regression. *Am. Stat.* **46**, 175–185 (1992).

35. E. O. Jones, O. Travis, P. Peterson, *SciPy: Open Source Scientific Tools for Python* (2001); www.scipy.org.

36. J. D. Hunter, Matplotlib: A 2D graphics environment. *Comput. Sci. Eng.* **9**, 90–95 (2007).

37. C. F. F. Karney, Algorithms for geodesics. *J. Geodesy* **87**, 43–55 (2013).

38. E. D. Fraenkel, thesis, University of Groningen (2014).